Journal of Materials Chemistry C

Accepted Manuscript

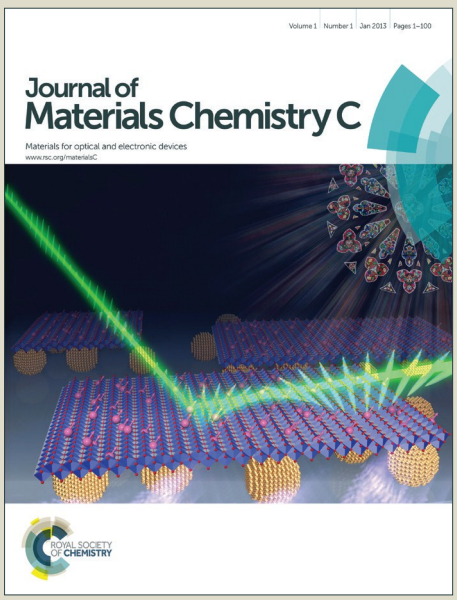

ROYAL SOCIETY OF CHEMISTRY

www.rsc.org/materialsC

Manipulation of the fluorescence of nanocrystals by opal-based heterostructures

Bourdillon Céline[a,b], Hong Phan Ngoc[c], Daney de Marcillac Willy[a,b], Coolen Laurent[a,b], Maître Agnès[a,b], Schwob Catherine[a,b].

Received (in XXX, XXX) XthXXXXXXXXX 20XX, Accepted Xth XXXXXXXXX 20XX
DOI: 10.1039/b000000x

Opal-based photonic crystals are promising materials to engineer complex heterostructures for efficient manipulation of nano-emitters fluorescence. We fabricated and characterized a structure composed of a layer of silica embedded between two silica opals. Thanks to this controlled planar defect which opens a permitted frequency band in the photonic stopband, an increase of emission, depending on angular distribution, is evidenced through photoluminescence spectroscopy. We discuss the use of such a structure as a self-assembled micrometer-sized spectroscopic device and demonstrate that it can be used to point the maximum emission wavelength of an unknown light source up to a certain linewidth. It can as well separate two sources, emitting at different wavelengths, with a resolution given by the Rayleigh criterion.

Introduction

Because they offer particular optical properties, such as photonic bandgaps, photonic crystals are intensively developed and studied.[1] They are defined by a periodicity of the optical index at a scale comparable to the optical wavelength, in 1, 2 or 3 dimensions[1], and can be fabricated by various techniques. Lithographic techniques are the most used to engineer 1D- and 2D-photonic crystals. They can also provide complex and versatile 3D-photonic crystals[2-5] but at the cost of heavy and long processes, leading to small size samples. An alternative consists in processes based on the self-assembly of colloidal nanospheres solutions such as sedimentation[3,4], Langmuir[5,6] or convective methods[7,8]. The resulting 3D-photonic crystals composed of compact stackings of silica or polymer spheres, also called opals, present a well-defined face-centered cubic crystalline structure over centimetre scales.

The periodicity of an opal can be disrupted by the introduction of a controlled defect in the structure, which opens a permitted band in the forbidden photonic stopband. Various techniques[9] have been developed to engineer defects in opals. Among them, the integration of a planar defect, made by Langmuir methods[5,6,10] or material sputtering[11], has been successfully realized.

Photonic crystals, and particularly opals, are of great interest to modify the emission properties of fluorescent nanoparticles such as organic molecules[12–14] or quantum dots[13,15,16]. Indeed, when the emission wavelength of the emitter corresponds to the stopband, the emission intensity can be strongly decreased[17,18] and the fluorescence lifetime can increase[17–20]. In literature, opals were also used in plasmonic devices to manipulate light properties: as templates to fabricate a plasmonic grating[21,22], as hybrid photonic-plasmonic crystals[23] or coupled to metallic quantum dots[24]. Moreover, the modification of the opal reflexion properties due to pressure, temperature, chemical or biological stimuli can be used to create a sensor, and integration of nanocrystals in opals has been suggested in order to create active sensor materials.[25]

In this paper, we present an efficient method to angularly filter the fluorescence of colloidal nanocrystals with an opal-based heterostructure, composed of a layer of sputtered silica between two silica opals. We demonstrate, by measurements of emission diagrams, that the photonic crystal affects the detected fluorescence of nanocrystals. The use of such a structure for the spectral determination of one or two unknown light sources is discussed. Its ability to be used as a filter device is evaluated in terms of resolution.

Synthesis and characterization of the opal-based heterostructure

The hererostructure of interest is composed of a planar defect sandwiched between two silica opals. The opals are fabricated by self-assembly from home-made silica spheres. The spheres are synthetized using a procedure derived from the Stöber-Fink-Bohn method[26]: as published previously[27], we obtain spherical and uniform particles with a mean diameter of 343 nm and a size dispersion of 5.7%. The self-assembly technique used to prepare the opals from these spheres is the convective method.[7] In this method, a substrate, tilted with an angle of 10° with respect to the vertical direction, is placed in a vessel containing a colloidal solution of silica spheres at a concentration of 2%w/v in ethanol. A temperature gradient, applied between the bottom of the vessel and the surface of the solution, facilitates the evaporation of the solvent, leading to a convective motion which brings the spheres to the meniscus where they self-organize. With the chosen parameters, we obtain well-ordered crystallographic structures, as demonstrated by the different crystallographic planes visible on Figure 1. The opal thickness is of the order of 12 layers (4.1 μm).

Figure 1. SEM images of a cross section a- of the opal-silica layer-opal heterostructure, b- with a zoom on the defect mode before the deposition of the upper opal.

The planar defect is obtained by deposition of a given thickness of silica on the surface of an opal[11]. Silica (with optical index equal 1.49) was sputtered from a SiO_2 target under argon atmosphere. The opal surface was oriented to be parallel to the target so that the sputtering took place with a preferred direction, perpendicularly to the surface. The parameters which influence the crystallinity and the thickness of the sputtered layer are the nature of the gas, the resulting pressure in the deposition chamber, the temperature of the substrate, the distance between the silica target and the substrate (which has to be slightly larger than the mean free path of the silica particles) and the duration of the process. We worked with a residual pressure of argon of 10^{-3} mbar, which corresponded to a mean free path between 5 and 6 cm. Consequently, the distance between the target and the substrate was set to 6 cm. The temperature of the substrate was on the order of 100°C (0.07 times the fusion temperature of silica). Under these sputtering conditions, the deposited silica forms columns on top of the spheres of the opal upper layer, leading to a structure that reproduces the opal periodicity (fig. 1b). To complete the heterostructure, the sputtered silica layer is covered by a second opal similar to the first one. As it induces a disruption of the opal periodicity in the thickness direction, the planar defect creates a frequency passband inside the opal photonic bandgap, analog to the role of defects in crystalline solids.[28] In other words, the silica layer constitutes an optical Fabry Perot-like cavity, with the opals in their forbidden band acting as mirrors. At the output of the cavity, maxima of transmitted light are obtained for the corresponding wavelengths. The spectral position of the passband depends on the thickness of sputtered silica (see simulations in the supporting information part). For the sample studied here, the thickness *e* of the defect layer, determined from SEM images as the height of the elongated beads minus the opal spheres diameter (fig. 1b), is 112 nm.

The heterostructure was optically characterized by angle-resolved specular reflection spectroscopy.[29]

The spectra were recorded, from the air–opal interface, at various incidence angles θ, defined from the normal to the (111) crystallographic planes (sample surface). The incident beam was provided by a supercontinuum source connected to an optical fiber, mounted on a goniometer arm with a collimator to obtain a light spot of 2 mm on the sample. The reflected beam was collected by a symmetric collimated fiber. The detected signal was analysed by a spectrometer (resolution $\Delta\lambda$= 1.5 nm). All spectra were normalized by the source spectrum, measured with the two fibers facing each other. As the incident light was unpolarized, the detected signal included both s- and p-polarizations.

Figure 2. Specular reflection spectra of the heterostructure at different angles θ.

Figure 2 shows the reflection spectra for specular angles θ ranging from 15° to 45°. For each angle the signal displays a sharp dip of 20 nm Full Width at Half Maximum (FWHM) (shown with dotted lines for the 20°-spectrum on Figure 2) corresponding to the defect mode caused by the planar defect (passband and so increase of the transmitted light), within a broader peak which is the signature of the opal stopband. Indeed, if a wavelength of the white source spectra is located in the stopband, the corresponding light cannot propagate through the photonic crystal and is consequently reflected. As opals present incomplete bandgaps (light propagation is not forbidden for all directions), the reflected wavelengths depend on the angle and follow approximatively Bragg's law. The defect mode dip is shifted to shorter wavelengths, when the angle θ increases, as expected in a Fabry Perot-like cavity. The thickness of the sputtered silica layer was chosen so that the defect mode was located in the middle of the stopband. To quantify the depth of the defect mode, we defined the figure of merit F of the heterostructure as $F= (R_{max} - R_{min})/(R_{max} + R_{min})$, R_{max} and R_{min} being respectively the reflection maximum of the spectrum and the minimum of reflection corresponding to the defect mode. The high measured value of F, F~45% is an indication of the heterostructure good quality and in particular of the epitaxial growth of the second opal on top of the first one.[11]

Figure 3. Plot of the wavelengths of the defect mode dips in reflection measurements (black squares) and peaks in fluorescence measurements (red points) as a function of the specular or collection angle respectively.

On Figure 3, we plot the central wavelength of the defect mode for both reflectance and fluorescence (presented in the next part) measurements as a function of the angle θ. By varying θ from 15° to 57.5°, this one can be tuned over more than 150 nm. We establish here a clear relationship between the central wavelength of the passband and the angle θ. We will use it, in the last part of this article, to convert the angles obtained by emission diagrams measurements into wavelengths.

Angle-resolved photoluminescence spectro-goniometry

The opal-based heterostructure was used to manipulate the fluorescence of colloidal semi-conductor CdTeSe/ZnS core-shell nanocrystals with a fluorescence maximum at 705 nm and a full width at half maximum of 60 nm. Its effects on emission were evidenced by photoluminescence spectro-goniometry.

The experimental setup is presented on Figure 4. A 3µl dropplet of 1µM solution of nanocrystals in decane was spread on a glass slide. After solvent evaporation, the heterostructure described above was placed on the slide. The nano-emitters were pumped by a cw blue laser diode (wavelength 473 nm, power 100 mW) at fixed incidence. The fluorescence transmitted through the heterostructure was collected by an optical fiber mounted on a rotation stage to change the angle of detection θ (with respect to vertical direction normal to the sample)[18]. The distance

between the sample and the fiber was around 10 cm, the size of the illumination spot, 25mm^2, and the angular resolution, approximately 3°. The signal was analysed with a spectrometer (Jobin Yvon HR460) coupled to a nitrogen-cooled Si-CCD camera. The spectral resolution of the setup was 1 nm.

Figure 4. Experimental setup (top) and emission spectra (down) of the nanocrystals through an opal with defect mode (named heterostructure sample) and an opal without defect mode (named reference sample) for 20° and 60° angles.

Figure 4 shows the photoluminescence spectra recorded at various θ angles through the heterostructure sample (planar defect between two opals) and through a single opal without planar defect, used as a reference sample. The spectra were centered at 705 nm and their differences in intensity and shape originated from the stopband and passband (defect mode) effects which spatially and spectrally filter the emission.

A clearer representation consists in plotting the emission diagram, the collected intensity as a function of the angle for a given emission wavelength. Figure 5(a) shows the emission diagram at 690 nm for θ ranging from 0° to 90° for the heterostructure sample and the reference sample.

Figure 5. a- Angular emission of the nanocrystals through the heterostructure sample (plain line) and the reference sample (dotted line) at 690 nm. b- Angular emission of the nanocrystals through the heterostructure sample normalized by the emission through the reference sample at different wavelengths (1: 710 nm, 2: 700 nm, 3: 690 nm, 4: 680 nm, 5: 670 nm).

At large angles (90°), for both samples, the collected fluorescence was very low and increased as the angle decreased due to the Lambertian nature of the emission diagram. For angles between 40° and 0°, the emission diagram differed from a Lambertian one: a large dip in the fluorescence intensity, corresponding to the photonic bandgap, was observed. For the heterostructure sample, a sharper peak (roughly 15° of angular width) appeared in the dip evidencing the passband induced by the planar defect.

To highlight this fluorescence peak, we plot on Figure 5b the emission through the heterostructure normalized by the emission through the reference sample at the same wavelength, for different wavelengths in the stopband of the opal. The passband signature appeared clearly as a sharp peak. For high angles (larger than 40°), the ratio between the two signals was almost constant and close to one (it decreased above 80° due to normalization between two vanishing signals). A slight dip can be observed on both sides of the peak. It comes from the fact that the stopband width is larger in the case of the heterostructure (as it can be observed on Figure 5a): this leads to a normalization with an artificially high value of the signal, and so to the appearance of a dip.

The angular positions of the maxima of fluorescence for different wavelengths (Figure 5b) are in very good agreement with the minima of reflection (Figure 2), as evidenced by the plot of the central wavelengths, for both fluorescence peaks and reflection dips, as a function of the angle θ, shown of Figure 3. This allows a direct conversion between angular and spectral positions from the experimental values.

We demonstrated that this opal-based heterostructure is an interesting tool for an efficient spectrally-dependent angular filtering of the emission of nanocrystals.

Light sources characterization

In this part, we show, through the exploitation of the experimental emission diagrams, that the opal-based heterostructure can provide an efficient micrometer-size spectroscopic device, leading to a spectral information on different kinds of light sources. Moreover, we demonstrate that this structure can be used to spatially separate two sources, emitting at different wavelengths, and we evaluate the corresponding resolution.

Determination of the central wavelength of a light source

The photoluminescence experiments shown on Figure 5 were obtained with 60 nm-spectral width nanocrystals and analysed with a 1 nm resolution, leading to emission diagrams recorded each nm. From these experimental results, we evidenced a clear relationship between the angle θ_c corresponding to the maximum of the fluorescence peak and the wavelength λ_c corresponding to the maximum of the reflection dip.

We want now to extract a spectral information from a broad light source by summing the recorded emission diagrams at different wavelengths. This is equivalent to measuring the light transmitted by a broad source through the heterostructure in the far field on a simple CCD camera.

The photoluminescence measurements allow us to determine the emission diagram when the heterostructure is illuminated by a Gaussian source of variable spectral width δλ. Details on the reconstructed fluorescence intensity are given in the supporting information part.

We plot on Figure 6 the reconstructed signal for different widths of the light source.

Figure 6. Reconstructed normalized angular emission for a source of gaussian spectrum centered at 690 nm and different δλ= 1.2nm, 12nm, 24nm, 36nm, 48nm, 60nm, 71nm.

We can point the maximum of the fluorescence peak, and so deduce the spectral position of the maximum from the reconstructed emission diagram. We measure a value of the angle θ_c of 21° (with ±3° resolution, due to the photoluminescence experimental setup) and recover the expected value of the central wavelength of the light source λ_c =690 nm (with ±15 nm resolution) from the relationship established in Figure 3. This method can be used as long as the source width is not too broad compared to the defect mode width. Indeed it is applicable up to 60 nm-FWHM light sources.

Spectral resolution for a superposition of two light sources

In the previous part, we have shown that the emission diagrams of nanocrystals could be used to determine the

central wavelength of a light source until a critical width. In this part, we consider the case of a mixture of two kinds of fluorophores, emitting at different wavelengths, and demonstrate that they can be spectrally resolved thanks to their fluorescence diagrams recorded through the heterostructure. As previously, we consider, two sources with central wavelengths λ_1 and λ_2 and widths $\delta\lambda_1$ and $\delta\lambda_2$ respectively, separated by $\Delta\lambda$ ($\Delta\lambda=|\lambda_2-\lambda_1|$). By summing the corresponding reconstructed emission diagrams, we obtained the angular response of the two mixed sources. On Figure 7, we plotted the emission diagrams for a source width $\delta\lambda$=1.2 nm and different $\Delta\lambda$ decreasing from 40 nm (Figure 7a) to 20 nm (Figure 7c).

Figure 7. Reconstructed angular emission diagrams of the 1.2 nm-width sources (red and blue lines) and the sum (black line) of the diagrams for different $\Delta\lambda$: a- $\Delta\lambda$=40nm; b- $\Delta\lambda$=25nm; c- $\Delta\lambda$=20nm

The two sources contributions can be distinguished on the emission diagrams if the central wavelengths are separated by at least 25 nm.

Finally, the sources widths were expanded to 12 nm, 24 nm and 36 nm to compare with the sharper ones. For each width, we plotted on Figure 8, the emission diagrams corresponding to the resolution limit $\Delta\lambda_{min}$.

Figure 8. Reconstructed angular emission diagrams (red and blue lines) and the sum (black line) of the emission diagrams of two sources of different $\delta\lambda$ at the corresponding $\Delta\lambda_{min}$: a- $\delta\lambda$=12nm, $\Delta\lambda_{min}$=25nm ; b- $\delta\lambda$=24nm, $\Delta\lambda_{min}$=30nm; c- $\delta\lambda$=36nm, $\Delta\lambda_{min}$=40nm.

For quasi-monochromatic sources ($\delta\lambda$=1.2 nm and $\delta\lambda$=12nm), sharper than the defect mode FWHM (20 nm, see Figure 2), the resolution is limited by the heterostructure and is equal to $\Delta\lambda_{lim}$=25 nm. For broader sources ($\delta\lambda$=24 nm and $\delta\lambda$=36 nm), larger than the defect mode FWHM, the resolution is limited by the source and given by the Rayleigh criterion. Finally, we could distinguish sources of maximum widths equal to 36 nm, separated by at least 40 nm. In the case of two sources of different widths, the resolution limit is given by the larger source.

Conclusion

Opal-based heterostructures are efficient tools to manipulate the fluorescence of nano-emitters. We demonstrated a significant angular filtering of the emission through emission diagrams inferred from photoluminescence spectroscopy. From the experimental data, we proposed an original use of these structures, as a self-organized micrometer-sized monochromating device, to determine the central wavelength of an unknown light source, from the knowledge of the angular position of the fluorescence peak. With this method, light sources as broad as 60 nm-FWHM can be characterized. We also studied the case of two mixed unknown light sources and shown that they can be distinguished until a 36 nm-FWHM with a resolution limit of 40 nm. Coupled to a simple camera, these structures can provide an efficient device for spectral characterization.

Supporting information

Simulation of the heterostructure

To achieve a complete study of the heterostructure, we simulated the 0°-transmission spectra (instead of reflection spectra for computing power reasons) of our samples illuminated by a light source of constant intensity over the visible range. Simulations have been performed with the Finite Difference Time Domain (FDTD) method, using the freely available software MEEP developed in MIT.[30] The computed structure is shown on the inset of Figure 9. For the lower and upper opals, the spheres diameter and silica index values, deduced from structural and optical characterizations[29], were set respectively to D=343 nm and n_1=1.32. To reproduce the shape of the defect made of sputtered silica, a monolayer of spheres of same diameter D and of index n_2=1.49 was inserted between the two opals (n_1 is lower than n_2 because of the porosity of the silica spheres synthetized by sol-gel method). The position of these spheres was set so that the distance between their top and the top of the first opal upper layer was equal to the thickness *e* of sputtered silica measured by SEM (Figure 1b). Moreover, to obtain a computed structure as close as possible to real sample, we needed to fill the voids between the two kinds of spheres of the model. For this, we added a rectangular layer of index n_2 and of width *e* between the centers of the two layers.

Figure 9: Top: Schematic of the computed structure. Down: 0°-transmission spectra for an opal without defect (black line) and with defects of different thicknesses (red line: 50 nm, blue line: 112 nm, green line: 150 nm).

On Figure 9, we plotted the 0°-transmitted spectra for a 24 layers-opal without planar defect and for heterostructures with different values of the defect thickness *e*, ranging from 50 nm to 150 nm. One can observe a broad dip of transmission, corresponding to the peak of reflection on experimental reflection spectra, which is the signature of the photonic stopband. Inside this broad dip, a sharper peak (corresponding to an increase of the transmission) appears if a defect layer is embedded between the two opals. It corresponds to the passband created by the disruption of the

opal periodicity due to the defect layer. For *e*=112 nm, the defect layer thickness measured on the studied heterostructure, the defect mode is perfectly centered on the stopband as observed on reflection spectra for the real sample. By changing the value of *e*, its spectral position can be tuned inside de stopband.

Construction of the broad light source

We consider a Gaussian source $S(\lambda)$ with a full width at half maximum $\delta\lambda$ centered on λ_c=690 nm which illuminates the sample and reconstruct the corresponding fluorescence intensity as:

$$I_{reconst}(\theta) = \sum_{\lambda} I_{meas}(\lambda,\theta) \times \frac{S(\lambda)}{I_{meas}(\lambda, 60°)}$$

In this relationship, $I_{meas}(\lambda,\theta)$ corresponds to the experimental emission diagrams, $I_{meas}(\lambda,60°)$ to the experimental emission diagrams at 60°, far from the stopband of the opal (see Figure 4), and it is used for normalization by the CdTeSe/ZnS nanocrystals intrinsic spectrum.

The reconstructed signal is normalized by the same signal, $I_{reconst}(\theta)$, in the case of the reference sample (opal without planar defect).

Acknowledgments

The authors would like to thank their colleagues from INSP, Dominique Demaille for SEM measurements and Stéphane Chenot for silica sputtering.

The collaboration between INSP and IMS was supported by a Projet International de Coopération Scientifique (PICS 5724) between CNRS and VAST.

This work was supported by French state funds managed by the ANR within the Investissements d'Avenir programme under reference ANR-11-IDEX-0004-02, and more specifically within the framework of the Cluster of Excellence MATISSE and by the Direction Générale des Armées (ANR-DGA "Calypso" and part of the financial support of Céline Bourdillon's PhD).

Notes and references

[a] *Sorbonne Universités, UPMC Univ Paris 06, UMR 7588, INSP, F-75005, Paris, France*
[b] *CNRS, UMR 7588, Institut des NanoSciences de Paris, F-75005, Paris, France*
schwob@insp.jussieu.fr
[c] *Institute of Materials Science, Vietnam Academy of Science and Technology, 18 Hoang Quoc Viet road, Cau Giay distr., Hanoi, Vietnam*

1 C. López, *Adv. Mater.*, 2003, **15**, 1679–1704.

2 M. Campbell, D. N. Sharp, M. T. Harrison, R. G. Denning and A. J. Turberfield, *Nature*, 2000, **404**, 53–56.

3 G. Subramanian, V. N. Manoharan, J. D. Thorne and D. J. Pine, *Adv. Mater.*, 1999, **11**, 1261–1265.

4 B. T. Holland, C. F. Blanford and A. Stein, *Science*, 1998, **281**, 538–540.

5 P. Massé, S. Reculusa, K. Clays and S. Ravaine, *Chem. Phys. Lett.*, 2006, **422**, 251–255.

6 J.-F. Dechézelles, T. Aubert, F. Grasset, S. Cordier, C. Barthou, C. Schwob, A. Maître, R. A. L. Vallée, H. Cramail and S. Ravaine, *Phys. Chem. Chem. Phys.*, 2010, **12**, 11993–11999.

7 P. Jiang, J. F. Bertone, K. S. Hwang and V. L. Colvin, *Chem. Mater.*, 1999, **11**, 2132–2140.

8 H. Cong and W. Cao, *Langmuir*, 2003, **19**, 8177–8181.

9 P. V. Braun, S. A. Rinne and F. García-Santamaría, *Adv. Mater.*, 2006, **18**, 2665–2678.

10 P. N. Hong, P. Bénalloul, Z. Guennouni-Assimi, R. Farha, C. Bourdillon, M.-C. Fauré, M. Goldmann, W. Marcillac, L. Coolen, A. Maître and C. Schwob, *Opt. Quantum Electron.*, 2014, 1–11.

11 P. N. Hong, P. Benalloul, L. Coolen, A. Maître and C. Schwob, *J. Mater. Chem. C*, 2013, **1**, 5381–5386.

12 E. P. Petrov, V. N. Bogomolov, I. I. Kalosha and S. V. Gaponenko, *Phys. Rev. Lett.*, 1998, **81**, 77–80.

13 S. V. Gaponenko, V. N. Bogomolov, E. P. Petrov, A. M. Kapitonov, D. A. Yarotsky, I. I. Kalosha, A. A. Eychmueller, A. L. Rogach, J. McGilp, U. Woggon and F. Gindele, *J. Light. Technol.*, 1999, **17**, 2128.

14 L. Bechger, P. Lodahl and W. L. Vos, *J. Phys. Chem. B*, 2005, **109**, 9980–9988.

15 Z.-Y. Li and Y. Xia, *Phys. Rev. A*, 2001, **63**, 043817.

16 M. Barth, R. Schuster, A. Gruber and F. Cichos, *Phys. Rev. Lett.*, 2006, **96**, 243902.

17 B. H. Husken, A. F. Koenderink and W. L. Vos, *J. Phys. Chem. C*, 2012, **117**, 3431–3439.

18 C. Vion, C. Barthou, P. Bénalloul, C. Schwob, L. Coolen, A. Gruzintev, G. Emel'chenko, V. Masalov, J.-M. Frigerio and A. Maître, *J. Appl. Phys.*, 2009, **105**, 113120.

19 M. D. Leistikow, A. P. Mosk, E. Yeganegi, S. R. Huisman, A. Lagendijk and W. L. Vos, *Phys. Rev. Lett.*, 2011, **107**, 193903.

20 Z.-Y. Li and Z.-Q. Zhang, *Phys. Rev. B*, 2001, **63**, 125106.

21 H. Frederich, F. Wen, J. Laverdant, L. Coolen, C. Schwob and A. Maître, *Opt. Express*, 2011, **19**, 24424.

22 H. Frederich, F. Wen, J. Laverdant, W. D. de Marcillac, C. Schwob, L. Coolen and A. Maître, *Plasmonics*, 2014, **9**, 917–924.

23 A. Hatef and M. R. Singh, *Phys. Rev. A*, 2010, **81**, 063816.

24 W. Wang and S. A. Asher, *J. Am. Chem. Soc.*, 2001, **123**, 12528–12535.

25 C. Fenzl, T. Hirsch and O. S. Wolfbeis, *Angew. Chem. Int. Ed.*, 2014, **53**, 3318–3335.

26 W. Stöber, A. Fink and E. Bohn, *J. Colloid Interface Sci.*, 1968, **26**, 62–69.

27 G. H. Bogush, M. A. Tracy and C. F. Zukoski IV, *J. Non-Cryst. Solids*, 1988, **104**, 95–106.

28 J. D. Joannopoulos, R. D. Meade and J. N. Winn, *Photonic Crystals: Molding the Flow of Light*, Princeton University Press, 1995.

29 A. Avoine, P. N. Hong, H. Frederich, J.-M. Frigerio, L. Coolen, C. Schwob, P. T. Nga, B. Gallas and A. Maître, *Phys. Rev. B*, 2012, **86**, 165432.

30 A. Taflove and S. C. Hagness, *Computational Electrodynamics: The Finite-Difference Time-Domain Method. Third edition*, Norwood MA, Artech House., 2005.

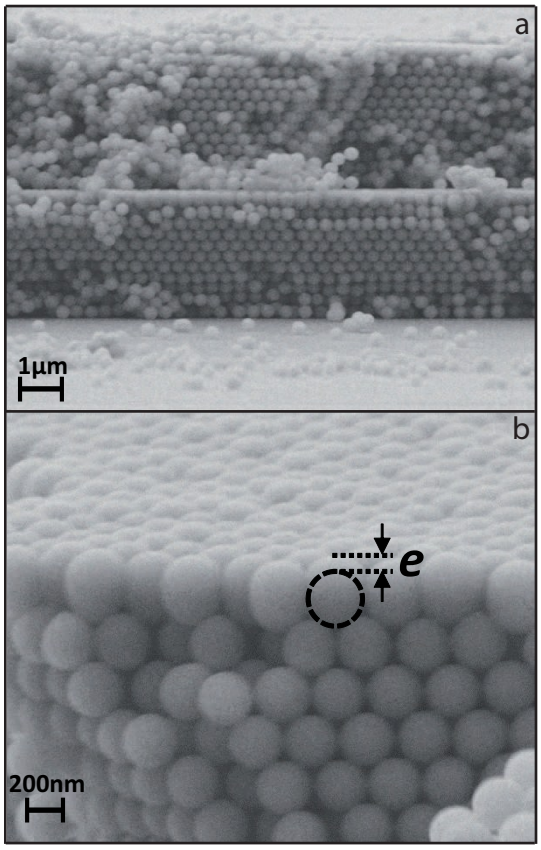

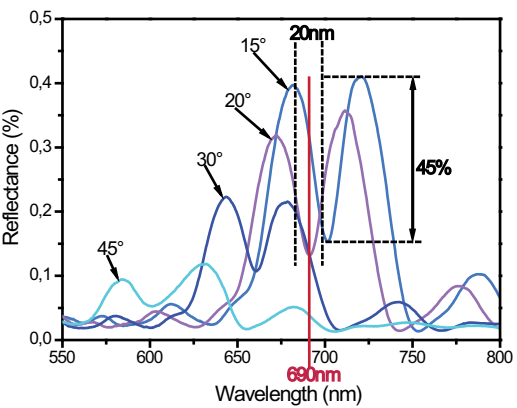

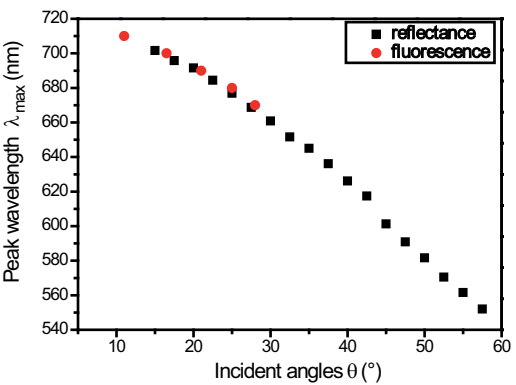

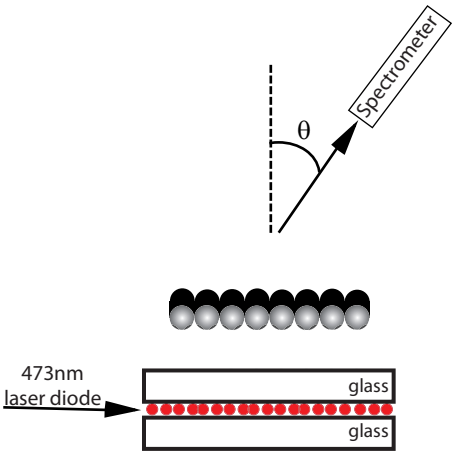

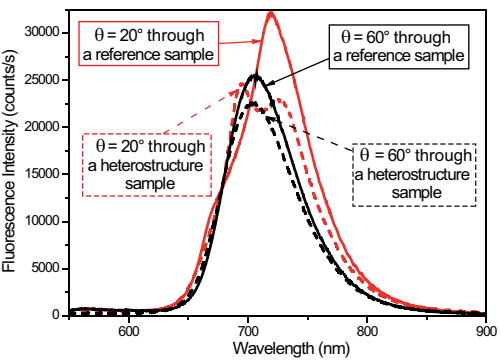

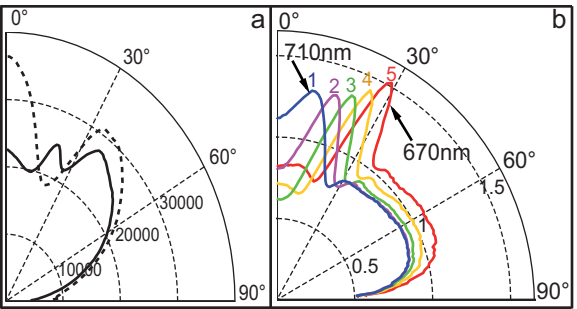

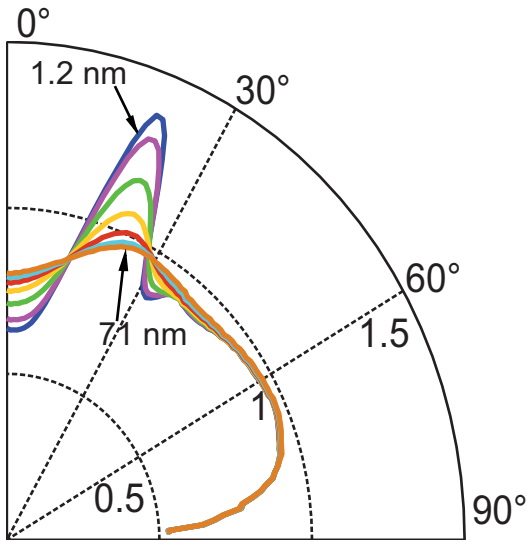

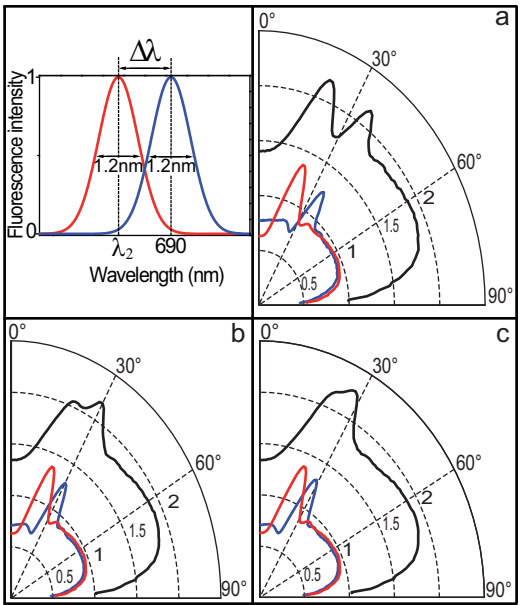

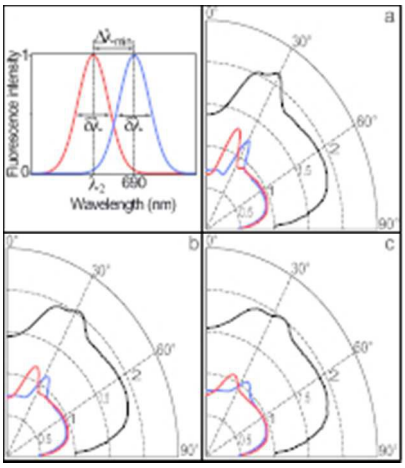

70x80mm (72 x 72 DPI)